ACS APPLIED MATERIALS & INTERFACES

Research Article

www.acsami.org

Graphene–Ionic Liquid Based Hybrid Nanomaterials as Novel Lubricant for Low Friction and Wear

Varsha Khare,* Minh-Quan Pham, Nitee Kumari, Hae-Sung Yoon, Chung-Soo Kim, Jae-IL Park, and Sung-Hoon Ahn*

School of Mechanical and Aerospace Engineering, Seoul National University, Gwanak-Ro 1, Gwanak-Gu, Seoul, 151-744, Korea

Supporting Information

ABSTRACT: Hybrid nanomaterials offer potential scope for an increasing number of novel applications when engineered to deliver usefully functional properties. Recent advancements in the design of new material products that result from interactions among different compositions at the nanoscale and microscale has led to innovative ways to fabricate and process hybrids with altered structural physicochemical properties. An example is the development of novel "lubricants" that make use of ionic liquids (ILs) and their ability to induce exploitable molecular assemblies at the IL–graphene interface. In the present study, we report the potential of graphene–IL hybrid nanomaterials for engineering applications with a focus on "lubricant" properties to reduce frictional forces to enhance tribological performance. The present contribution outlines the wear and tribological properties (friction and lubrication) of a highly viscous IL [BMIM][I] and its comparison with its nanohybrid material counterpart. Detailed structural–microstructural investigations of the nanohybrid materials were performed using X-ray diffraction and microscopic techniques employing scanning electron (SEM), transmission electron (TEM), and high resolution transmission electron (HRTEM) microscopies. A comparative study of the morphology of friction track and wear behavior was assessed by SEM and TEM. These characteristic properties within and outside the friction track were further correlated with physical and chemical interactions obtained by contact angle measurements and Raman spectroscopy and energy dispersive analysis by X-ray (EDAX).

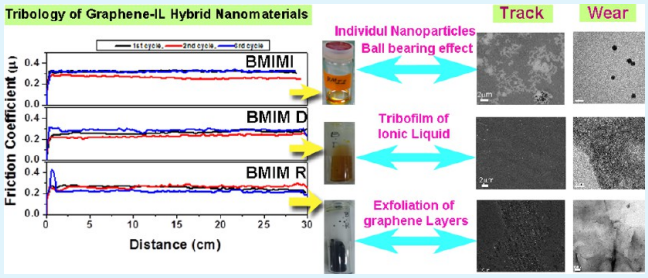

KEYWORDS: *graphene, ionic liquids, hybrid nanomaterials, lubrication, friction, wear*

1. INTRODUCTION

Energy consumption due to frictional wear is estimated to constitute typically 30–50% usage to overcome frictional forces as a result of interacting surfaces. Lubrication of surfaces therefore play a critical role in reducing wastage and increasing energy efficiency by decreasing production and manufacturing costs. The use of lubricants at the contact surface in mechanical processes has long been considered a key strategy in minimizing material and energy dissipation arising from frictional processes. However, equally important in maintaining mechanical durability with increased efficiency is selecting "well-suited" lubricant materials for a particular system.

The increasing importance of introducing environmentally friendly "green-based"' lubricants has also been a major concern. This has led researchers to explore a combination of material constituents that together impart increased wear and frictional resistance with environmentally friendly consequences. Ionic liquids (ILs) have been identified as a potential group of co-materials with advantageous physical and chemical properties for engineering applications.[1,2] Their inorganic/organic salt composition combining both anionic and cationic charged molecules, respectively, elicit numerable exploitable characteristics at room temperature such as broad thermal stability with nonflammability, a high electrochemical window, and their existence as liquid salts. In addition, the small vapor pressure associated with these salts is ideal for widespread use as a co-lubricant material ensuring their eco-friendly use as nonatmospheric pollutants. Negligible vapor pressure of ILs observed at room temperature is an intrinsic property that remains significantly low even at much higher temperatures. Triboheating due to friction affects the stability of conventional lubricants such as mineral oil, and therefore, this limitation is overcome by replacing them with ILs. This has been demonstrated by using long-chain 1,3-dialkyl imidazolium ILs which was found to function more effectively as a lubricant at 150 °C compared to room temperature[3] but also at moderate temperatures[4] and at extremely high temperatures[5] for steel–steel contacts. Such exploitable properties have led to their exploration for scientific and technological applications.

An alternative use of "anti-wear" chemical additives in lubricant materials such as viscosity modifiers to improve performance has in recent years shifted focus on the development of "nanolubricants" as nanofluids to exploit their superior properties. The realization of ILs as excellent

Received: November 20, 2012
Accepted: April 18, 2013
Published: April 18, 2013

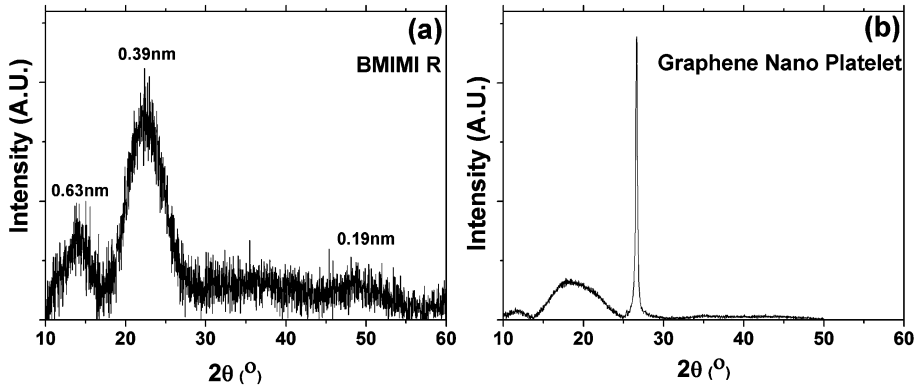

Figure 1. Typical X-ray diffraction pattern of (a) BMIMI R showing the presence of graphene with in-plane and interlayer defects. (b) Pristine GNP showing presence of nanosheets and large number of layers due to aggregation of platelets.

dispersants for the stabilization of well-characterized nanomaterials with a growing potential to function as lubricants offers exciting possibilities in the engineering field. Here, nanocomponents of hybrid nanomaterial–IL preparations aid lubrication by reducing friction coefficients (FC) and impart greater chemical/structural stability in the system through the formation of better wear resistant molecular arrangements as hybrids. For example, researchers have very recently demonstrated IL-assisted lubricant properties of nonfunctionalized single-walled carbon nanotubes on the friction and wear of amorphous polycarbonate. The authors report superior lubricant properties of low friction with the ability to prevent wear that directly result from newly formed surface interactions between carbon nanotubes and ILs.[6] Similarly, functionalized graphene–IL nanocomposite films with excellent lubrication properties have been proposed for use in nanomechanical applications.[7]

In the present study, we have produced a graphene–IL hybrid material based on 1-butyl-3-methylimidazolium iodide, i.e., [BMIM][I] using a facile synthesis route previously described.[8] Tribological investigations aimed to highlight its potential application as a lubricant for the reduction of friction and wear. Synthesis of the hybrid material offers an alternative to solid- and liquid-based lubricants that are disadvantaged by high temperature and high vacuum applications and limited anti-wear properties. The one-pot facile synthesis route employed here requires minimum energy input and operates with a FC superior to graphite for steel–aluminum contact.

2. EXPERIMENTAL SECTION

2.1. Preparation of Nanohybrid and Microhybrid Materials. Graphene–IL hybrid materials were prepared using the method established by Khare et al.[9] A mixture containing an appropriate amount of commercially available graphene platelets from xG Sciences (Lansing, MI) and commercially available [BMIM][I] IL from Io-li-tec (Heilbronn, Germany) was sonicated for 2 h followed by continuous mixing using a magnetic stirrer for 24 h. A stable dispersion visible as a blackish-green mixture composed of graphene/[BMIM][I] IL was seen to develop in the vial. As observed previously for gold and Fe_3C particles, a centrifugation step was applied to separate the colloidal phase (supernatant phase containing graphene nanoparticles named BMIMI D) and the sediment phase (BMIMI R containing the macro/microsized graphene particles). In order to visualize the difference in the three samples, photographs of pure IL, BMIMI D, and BMIMI R are shown in Figure S1 of the Supporting Information. In the present investigation, both phases were used as a lubricant to provide an overall assessment of the size effect on lubricating properties of the resulting hybrid material.

2.2. Structural–Microstructural Characterizations of Hybrid Materials. The gross structural information of graphene–IL hybrid materials were obtained by X-ray diffraction measurements using a Bruker D8 advanced with Cu Kα (λ = 1.542 Å) operated at 40 KV and 40 mA. Further, the detailed structural and microstructural characterization of the hybrid materials was performed by TEM using a Carl Zeiss energy-filtered transmission electron microscope (EF-TEM), LIBRA 120, operated at 120 KV. Further, in order to confirm the crystalline nature of wear particles, high resolution TEM (HRTEM) was performed using Technai F20 equipped with a double tilt holder arrangement.

After performing the friction tests using these hybrid materials as potential lubricants, the resulting friction tracks and wear particles were characterized by SEM using a Carl Zeiss field emission scanning electron microscope (FE-SEM) AURIGA.

2.3. Tribological Characterizations of Hybrid Materials. Friction and roughness measurements were performed using a Kawabata automated surface tester in the dynamic friction in sliding mode. A sample of dimension 20 cm × 20 cm was placed on a plate and run horizontally at the speed of 1 mm/sec. The dynamic friction was measured using a 1 point contact method with a 10 mm^2 frictional probe size directly connected to the detection unit by applying a 50 gf vertical load on the probe resulting in contact pressure of 20 gf/cm. During roughness measurements, the asperity height was measured all along the travel distance. A contact probe of 5 mm in length was applied perpendicularly on the samples with a 10 gf load. In a typical experiment in one run, the sample travels a distance of 30 mm in one direction and then returns to the original position. However, the friction and roughness sensor measures the average travel distance coverage of 20 mm by excluding a 5 mm distance on each end to account for transient data. The FC was measured averaging the absolute values in forward and backward strokes. Together with FC measurements, mean friction coefficient (MFC) data were also measured by removing low frequency components below 1 mm/sec from the FC output by filtering the friction measurements. MFC represents variations in friction resistance in the direction of travel whereas roughness represents the geometry of the surface. Typically in one cycle, the machine traveled three runs on the same position. Thus, one cycle covered a distance of 12 cm in forward and backward directions. In the present work, the measurements were done in three different cycles (cycles 1, 3, and 6) on different aluminum substrates of dimension 20 cm × 20 cm for the three lubricants. Furthermore, BMIMI R measurements were performed up to 18 cycles. The variation in FC, MFC, and roughness were measured for variable distances. The FC and roughness measurement was performed for a steel–aluminum contact using nanohybrid materials as lubricants.

3. RESULTS

3.1. Growth of Nanographene–IL Hybrid Material. The stable graphene and IL nanohybrid was synthesized via a dispersion route resulting in two distinct domains associated

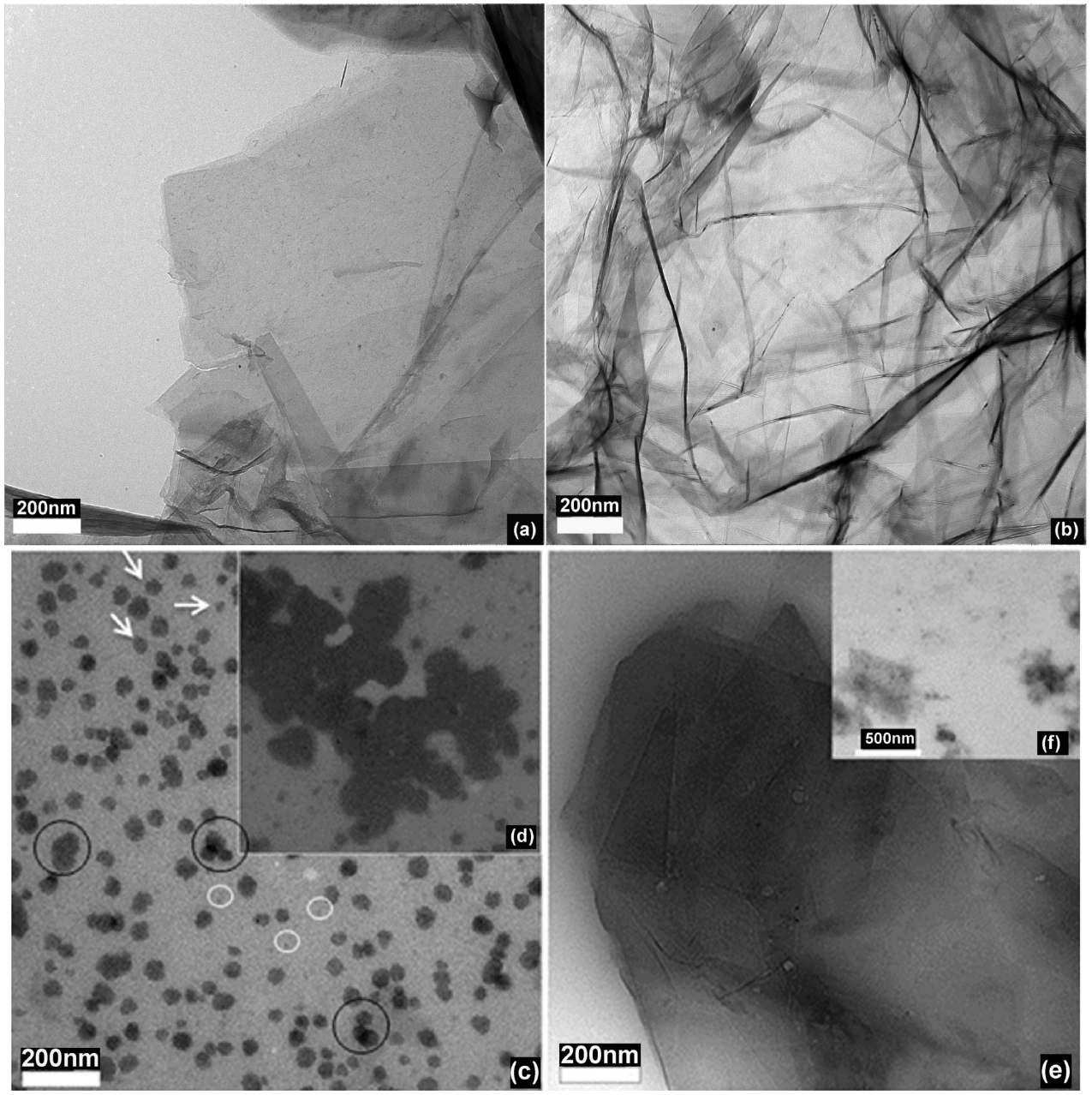

Figure 2. TEM Image (a),(b) of GNP showing characteristic microstructure of graphene. (c) BMIMI D showing the presence of nanoparticles of graphene (small white circles highlight the nuclei, and well-grown particles are indicated by white arrows, while coalescence of particle is shown within big black circles. (inset d) Aggregated nanoparticles. (e) BMIMI R exhibiting the graphene nanosheets. (inset f) Graphene nanoflakes embedded with graphene nanoparticles.

with the supernatant and sediment fractions. The supernatant fraction exhibits a colloidal suspension of graphene nanoparticles dispersed in IL (BMIMI D), while the sediment component generated larger flakes of graphene in IL (BMIMI R). The focus of the present work centers on the tribological performance of both nanohybrid regimes. Figure 1a is the representative X-ray diffraction pattern of BMIM R. The pronounced (002) peak is indicative of the presence of graphene, and the broad (002) peak signifies a low degree of crystallinity. The layer-by-layer distances were determined from the peak positions using $d = \lambda/2 \sin \theta$.

The d-spacing of 0.39 nm corresponding to the (002) peak marginally exceeds the interlayer spacing observed for graphite or pristine graphene and can be attributed to the presence of defects and the existence of the IL film between the two layers of graphene. Also, a weakly intense peak at $2\theta = 14.1°$ corresponding to an interlayer distance of 0.63 nm may arise from the presence of a few graphene layers. Furthermore, a rather weak and broad hump at $2\theta = 48.6°$ of 0.19 nm corresponding to the (100) peak of graphene was noted. This distance is slightly higher than the distance between the two carbon atoms of the in-plane honeycomb structure, which may result from possible defects produced by surface functionalization of graphene by IL ions. The broadness of the peaks suggests that the hybrid material of graphene exhibits in-plane and interlayer defects. Figure 1b represents the typical X-ray diffraction pattern of GNP, the initial material for hybrid material. The sharp and intense (002) peak at 26.5 corresponds

to the low defect nature of GNP. However, the broad reflection at 2θ = 18.3 indicates the presence of a few layer graphene.

The detailed microstructures of the respective nanohybrid materials BMIMI D and BMIMI R and GNP were obtained using TEM in the imaging mode. Figure 2 represents the typical electron micrograph of pristine GNP and the two nanohybrid materials. The few layer thickness (4−5 layers) of GNP is clearly discernible in the encircled region of Figure 2a. The electron micrograph shown in Figure 2b depicts the wrinkled morphology typical of graphene. These two micrographs represent the typical morphology of GNP we have used in the present study. Hybrid material "BMIMI D" forming the colloidal nanoparticles derived from the supernatant phase shows well dispersed nanoparticles possibly formed via a nucleation and growth process (Figure 2c) as reported previously for other ILs.[8] The nuclei in the range of 15−16 nm (white circles) and for the more well-grown particles of 20−70 nm were observed. Individual particles are also seen to coalesce to form particles from 100−150 nm to micrometer-sized colonies of nanoparticles (Figure 2d, inset). The much larger microstructural features of BMIMI R show the presence of thin flat graphene sheets of micrometer dimensions and nanometer thickness (Figure 2c). However, microsized sheets accompanied by nanosheets or flakes are also visible with the nanoparticles embedded in them (Figure 2f, inset). The individual nano/microsheets and nanoparticles within the sheets may have variable effects on the tribological performances of the nanohybrid materials.

Raman spectroscopy is a vital tool for the characterization of graphene samples. Figure 3 shows a comparative Raman

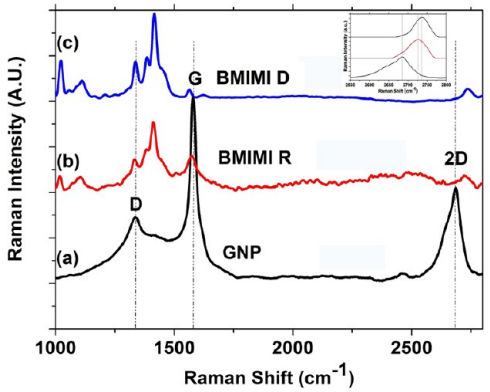

Figure 3. Comparative Raman spectrum of (a) GNP, (b) BMIMI R, and (c) BMIMI D indicating the presence of graphene in hybrid materials by the characteristic G and 2D peaks. Inset shows the variation in 2D peak position and asymmetry level. Color representation in inset is same as in main panel of figure.

spectrum of GNP (Figure 3a) and the two hybrid materials (Figure 3b,c). In all three samples, the material presence of graphene is discernible by the occurrence of G and 2D bands. The blue shift of the 2D band in the hybrid materials indicates the presence of strain due to the strong interaction between graphene and IL. Moreover, the intensity ratio of D and G bands changes significantly from GNP (∼ 0.35) to hybrid materials (BMIMI D ∼1.14 and BMIMI R ∼0.97). This variation suggests that in-plane defect concentration is increased in the hybrid material compositions. Asymmetry in 2D peaks of these materials shows the presence of multilayer graphene to a few layers of graphene. The inset suggests that the asymmetry decreases such that GNP exhibits maximum asymmetry, while BMIMI D shows minimum asymmetry, and this can be attributed to a decrease in the number of layers in BMIMI R and a further decrease in BMIMI D.

3.2. Assessment of Surface Energy Trends for Nanohybrid Materials. The reduction of friction and wear is related to the surface energy/hardness ratio of the contacting materials. Quantitative measurement of this ratio parameter is a technical challenge in relation to the friction and adhesion properties particularly with hybrid materials involving more than two contact surfaces. In terms of wear, it is more feasible to measure wear particle size, which is directly proportional to this ratio. Thus, in the present study, an indirect approach for the assessment of surface energy patterns for both nanohybrid materials was employed prior to tribological tests. Dynamic contact angle measurements were performed on the aluminum surface using the BMIMI (pure IL), BMIMI D, and BMIMIR. The droplet of the three materials spread on the aluminum substrate possibly due to chemical interaction at the surface or surface adsorption. Contact angle vs time curves for the three samples are shown in Figure 4. A comparison of the curves

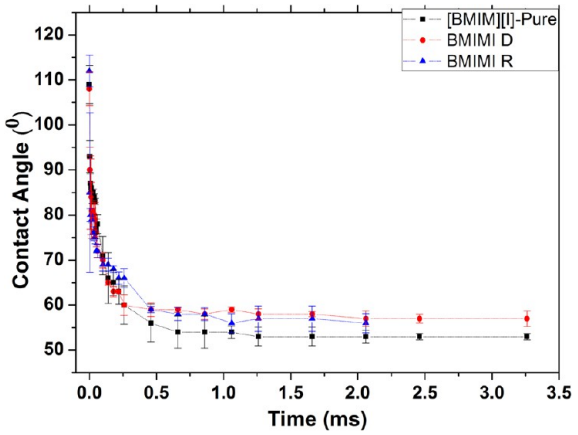

Figure 4. Contact angle vs time curves for BMIMI, BMIMI D, and BMIMI R indicating the highest surface energy for BMIMI.

suggests that pure IL appears to be associated with the highest surface energy indicated by the lowest contact angle. However, the contact angles of the two hybrid materials are relatively close to each other. Although the initial contact angle is highest for BMIMI R, it may be attributed to the lowest surface energy. It should be noted, however, that the contact angles are just trend predictors of surface energy. For quantitative surface energy measurements, methods that are more accurate are required and are the subject for future work.

3.3. Investigations of Tribological Performance of Nanohybrid Materials. Tribological behavior of the nanohybrid materials was examined at 50 gf load. The dynamic sliding friction measurements were performed with respect to the variable distance over several cycles. Variation in the friction coefficient with respect to the sliding distance for each cycle is shown in Figure 5. It was observed that the FC remains constant throughout the sliding distance with respect to all three materials for each cycle. This behavior is suggestive of the fact that the three samples are good candidates for reducing wear. However, it was noted that for BMIMI and BMIMI D, the friction coefficient decreases slightly up to cycle 2, but in cycle 3, the friction coefficient increases (Figure 5a,b).

dx.doi.org/10.1021/am302761c | ACS Appl. Mater. Interfaces 2013, 5, 4063−4075

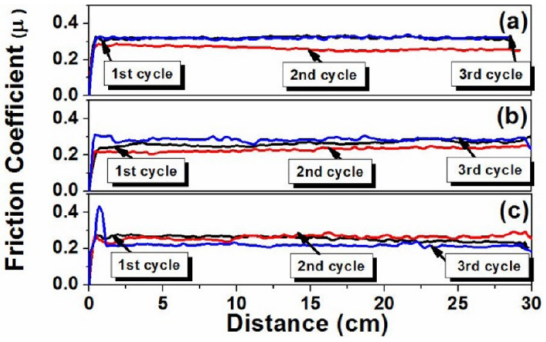

Figure 5. Friction coefficient vs distance curves of (a) BMIMI, (b) BMIMI D, and (c) BMIMI R indicating possibly the minimum wear and better friction coefficient for the hybrid nanomaterials. The curves are the measurements at the last run of cycle 3.

Reduction in friction coefficient can be related to the sliding distance and stability of the lubricating film composed of the IL−nanohybrid material on the aluminum surface. Furthermore in cycle 3, it is a possibility that the sliding distance is sufficiently high enough to destroy the film or some nano-asperities formed by the chemical or physical interactions between the IL and aluminum surface may be present. In contrast to BMIM I and BMIMI D, BMIMI R shows the minimum friction coefficient that occurs in cycle 3, which may be due to the presence of layered graphene sheets (Figure 5c). Furthermore, prolonged experiments on the BMIMI R sample exhibiting better friction behavior that persists at cycle 3 has been performed to understand the limit of reduced friction. Figure 6 is the comparative friction vs distance curve for various

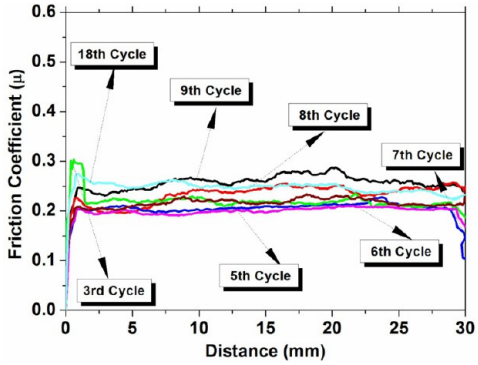

Figure 6. Friction coefficient vs distance curves of BMIMI R for longer cycles indicating the limit of reduction of friction. Measurements up to cycle 7 show a reduction in friction followed by an increase in the number of cycles, i.e., with distance.

cycles of BMIMI R. It is evident from Figure 6 that the sample sustains reduced friction up to cycle 7. After cycle 7, the increment in friction is discernible. The increment in friction after the cycle 7 shows graphene sheets exfoliated in small pieces that results in enhancement of the rough surface and hence increased friction. The FC with respect to the number of cycles and its correlation with MFC and surface roughness is shown in Figure 7. In Figure 7, samples are represented by symbols, and each color represents the number of cycles. It is evident from Figure 7 that the number of cycles and thus the sliding distance has significant effects on the friction of the nanohybrid materials used in the present investigations.

Detailed analysis of the three graphs (FC, MFC, and roughness) is shown in Figure 7a, b, and c depicting the frictional and lubrication behavior of the nanohybrid materials and the IL. In cycle 1, BMIM I show a linear increment in FC, MFC, and roughness, while for BMIMI D, the FC and MFC increases but surface roughness decreases drastically up to 8 cm followed by an incremental decrease observed from 8 to 12 cm. However, BMIMI R shows opposing behavior revealing a decrease in FC and MFC and a slight increase in the surface roughness. Interestingly, in cycle 2, when the repetitive sliding distance is increased up to 24 cm, BMIMI R compares poorly to BMIMI D, which shows superior FC and MFC properties despite presenting the highest surface roughness. In cycle 3, corresponding to the longest sliding distance, BMIMI R records the lowest FC and MFC indicating the lowest wear and surface roughness properties. With respect to BMIMI D, a large fluctuation in FC and MFC indicates a higher wear and lower anti-wear life of BMIMI D, which also affects surface roughness. In cycle 3, BMIMI shows the highest but stable FC, MFC, and surface roughness.

3.4. Surface Morphological Evolution within the Friction Track for Various Cycles. Variation in the tribological behavior of the three materials was further explored after friction measurements by monitoring microstructural changes using field emission scanning electron microscopy (FE-SEM) within the friction tracks. Figure 8 shows the FE-SEM images of three cycles of BMIMI (a, cycle 1; b, cycle 2; c, cycle 3) and BMIMI D (d, cycle 1; e, cycle 2; and f, cycle 3). The microstructure of BMIMI for all three cycles reveal the presence of micrometer-sized snowflake-like aggregates. The size and morphologies of the snowflakes changes as a function of cycle number. The images also show snowflakes accompanied by wear debris. In cycle 1, formation of micrometer-sized flat aggregates is clearly discernible in Figure 8a. However, along with the aggregate removal of material (wear particles), black spots are also visible that may be holes remaining after removal as seen by SEM. In cycle 2, relatively thin snowflakes are observed together with larger and thicker aggregates that are likely generated by the movement of nanoparticles within the IL. Nanoparticle formation is followed by bridging of larger nanoparticles, and large aggregates are formed through bridging of adjacent branches emerging from the body of the aggregates. The images finally show removal of loosely bound particles from the surface of the aggregates (inset I1, Figure 8b). With increasing frictional cycles occurring over longer distances, the resulting snowflake aggregations are dimensionally larger and thicker and appear brighter. The brighter contrast here is indicative of thickness increase. This likely occurs due to constant movements and is observed as bright white clusters. The background shows smaller nanoparticles that probably contribute to the assembly and thickness of flakes. Apart from this thicker wear debris, as shown in inset I2 of Figure 8c, smaller nanoparticles are also distributed within the microstructure. For BMIM D in cycle 1 (Figure 8d), wear debris appears as white particles along with the tribofilm partially covering the surface, but in the cycle 2 (Figure 8e), tribofilm is spread over larger areas, which may be the cause of relatively lower wear and lower surface roughness. Furthermore, in cycle 3 (Figure 8f), the rupture of the film appears in the form of a crack formation leading to greater concentration of thicker wear particles. Figure 9a and b shows the microstructure of the tribotrack for cycle 2 of BMIMI R indicating the presence of adhesion of the graphene flakes, nanocracks, and a relatively

dx.doi.org/10.1021/am302761c | ACS Appl. Mater. Interfaces 2013, 5, 4063−4075

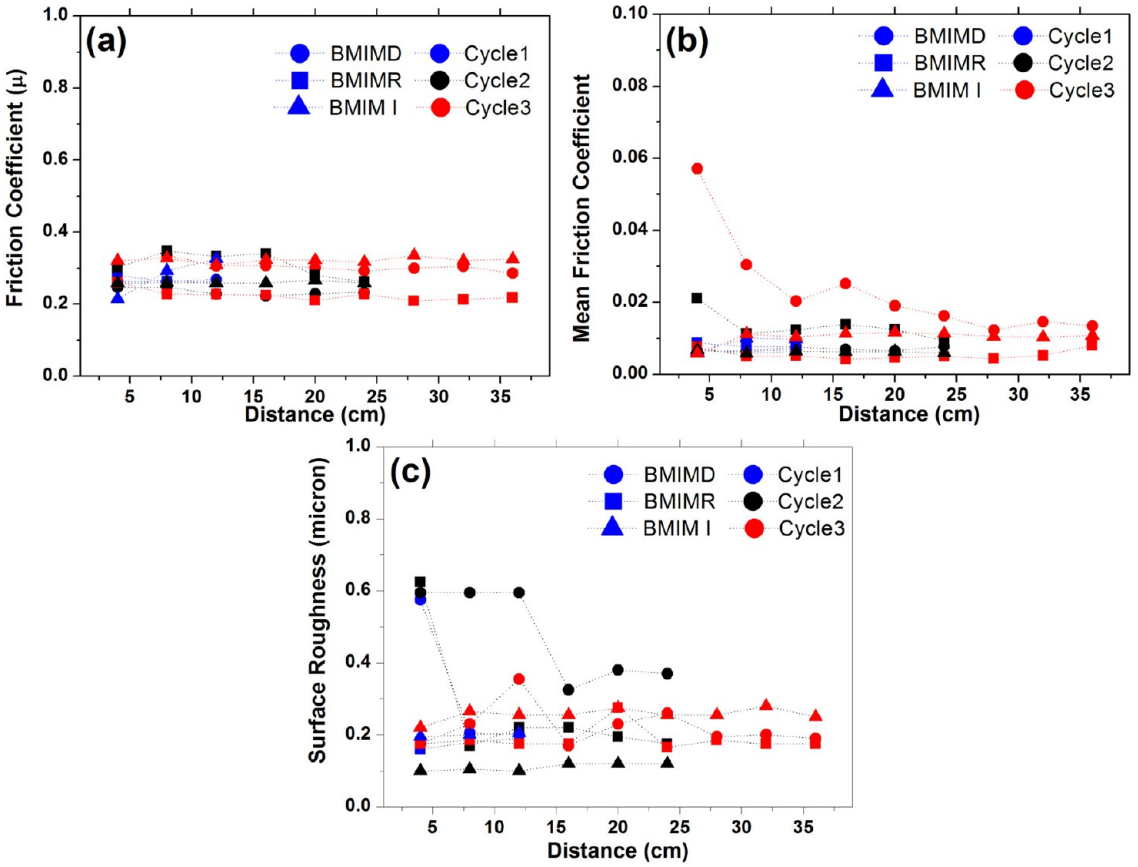

Figure 7. Comparative curve of friction coefficient, mean friction coefficient, and surface roughness for BMIMI, BMIMI D, and BMIMI R at the three difference cycles. The graphs show better correlation among the three independent variables.

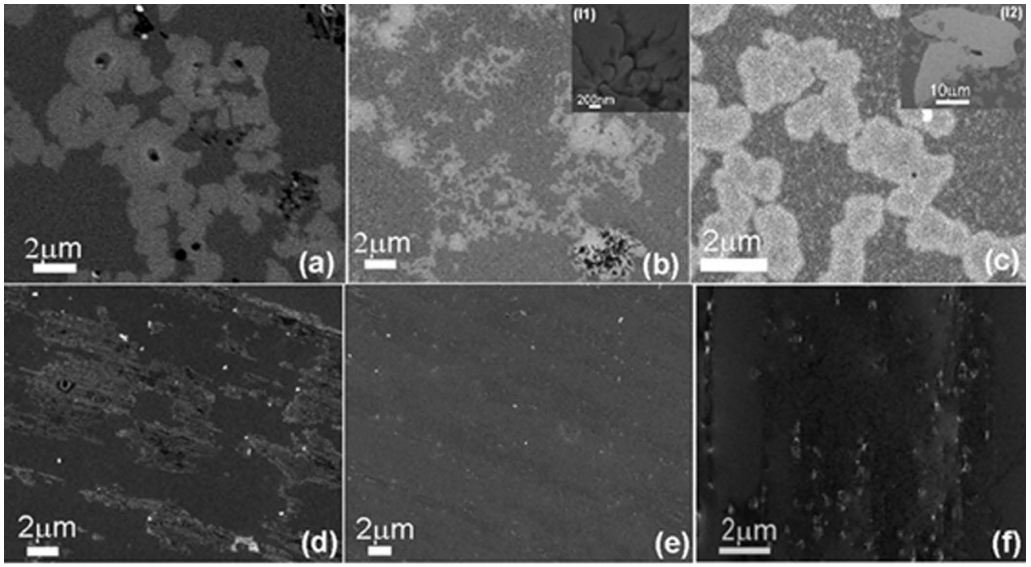

Figure 8. FE-SEM images of BMIMI (a) cycle 1 showing the snowflake-like flat aggregates with removed wear particles, (b) cycle 2 exhibiting thin snowflakes and bridged aggregates (inset I1) removal of loosely bound flakes, and (c) cycle 3 nanoparticles and thicker snowflake (inset I2) bigger needle shape wear particles. Images of BMIMI D (d) cycle 1 showing partial triboflim and wear debris, (e) cycle 2 spreading of tribofilm and decreased concentration of wear particles, and (f) cycle 3 rupture of film leading to cracks and large concentration of wear debris.

rough surface, which contributes to the high and unstable FC as shown in Figure 7. In cycle 3 (Figure 9c,d), BMIMI R shows the best tribological behavior and can be attributed to the tribofilm of liquid and graphene nanoflakes. The inset of Figure 9d indicates that the film of graphene flakes is relatively smooth and thus contributes to low friction. However, slight variation in the friction coefficients along the distance visible in Figures 5c and 6 may be due to the nanoscale roughness discernible in the inset. Figure 9e shows the rough surface of the track after cycle 9 is complete with the inset showing the porous

dx.doi.org/10.1021/am302761c | ACS Appl. Mater. Interfaces 2013, 5, 4063−4075

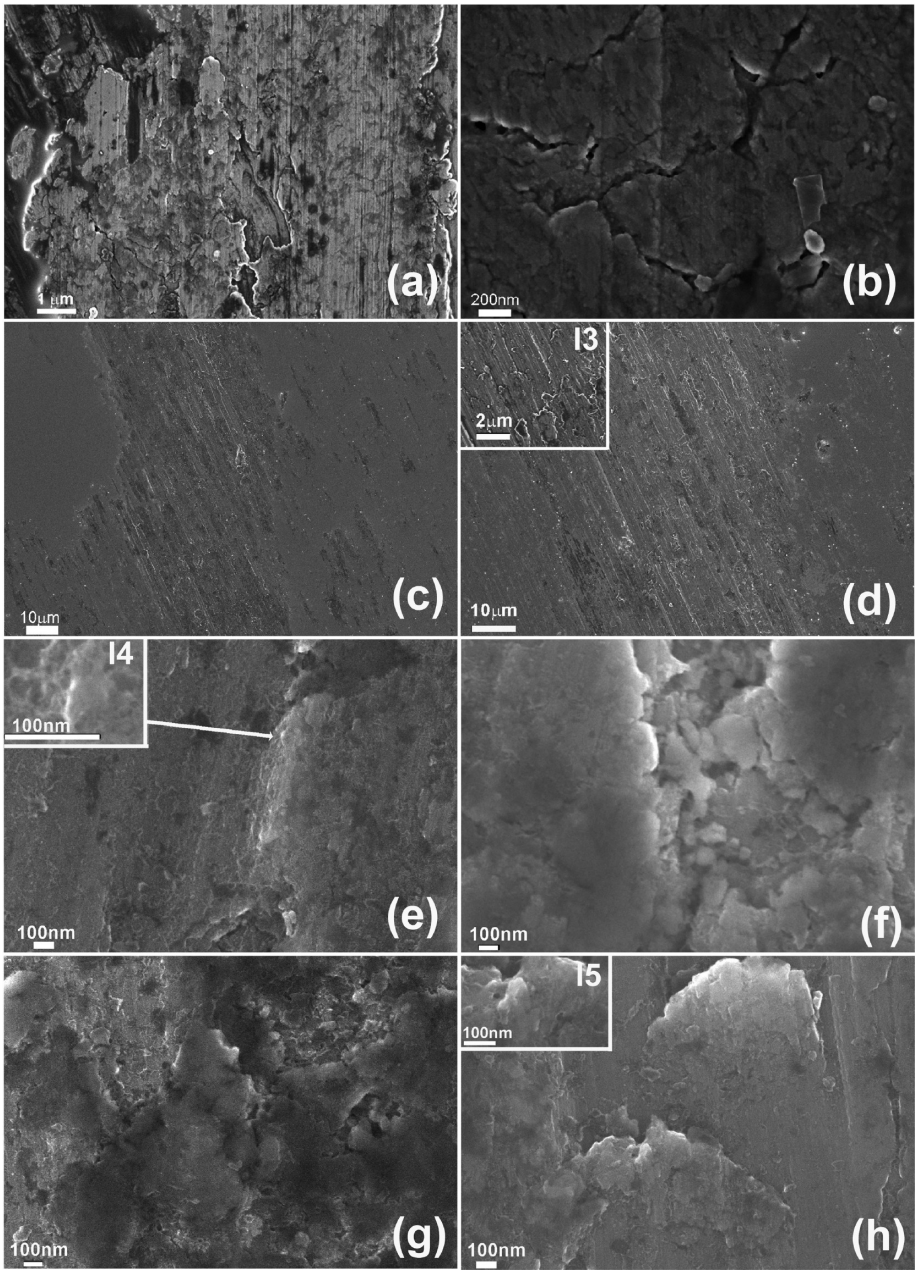

Figure 9. FE-SEM images of BMIMI R in cycle 2 showing (a) the rougher surface and (b) adhesion of graphene flakes with nanocracks. In cycle 3 (c) tribofilm of liquid, (d) graphene nanoflakes, and (inset I3) flattening of graphene flakes and thus forming a film on the surface. In cycle 9 (e), roughness of the surface (inset I4) in detailed view, originating from (f) rupture of film and further rupture and then adhesion of wear in (g) and (h). Detailed view of rupture is visible in inset I5.

microstructure of the surface. However, rupture of the film is clearly visible in Figure 9f. Furthermore, the surface roughness increases with distance as evident from the microstructure of the track at cycle 18. However, the adhesion of the wear debris shown in Figure 9h reduces the roughness and thus friction coefficient to slightly lower than that observed for cycle 9. Also, the roughness due to the porous microstructure for cycle 9 and due to further exfoliation of graphene flakes in the cycle 18 is clearly shown in Figure S3 of the Supporting Information. The presences of the two types of rough morphology explain the lowering of the friction coefficient in cycle 18.

3.5. Structural Information of Graphene within the Friction Tracks. In order to evaluate the effect of hybrid material on the wear and lubrication due to the formation of tribofilm of graphene, Raman spectroscopy was employed within the friction tracks. Figure 10 shows the Raman spectrum inside the friction track observed for BMIMI R, BMIMI D, and BMIMI after cycle 3. BMIMI R, which possesses superior tribological properties due to the formation of the tribofilm, suggests the presence of a few layered graphene. In the large area of the track, graphene was not covered by IL. A careful analysis of the Raman spectrum shown in Figure 10a and b indicates the presence of graphene within the friction track and helps in estimation of the number of layered sheets.[10−12] Graphene and graphite both have three representative bands D at 1350 cm^{-1}, G band at 1580 cm^{-1}, and an order−disorder 2D band. The shape of the 2D band is the determining factor for the number of graphene layers or presence of graphite. As

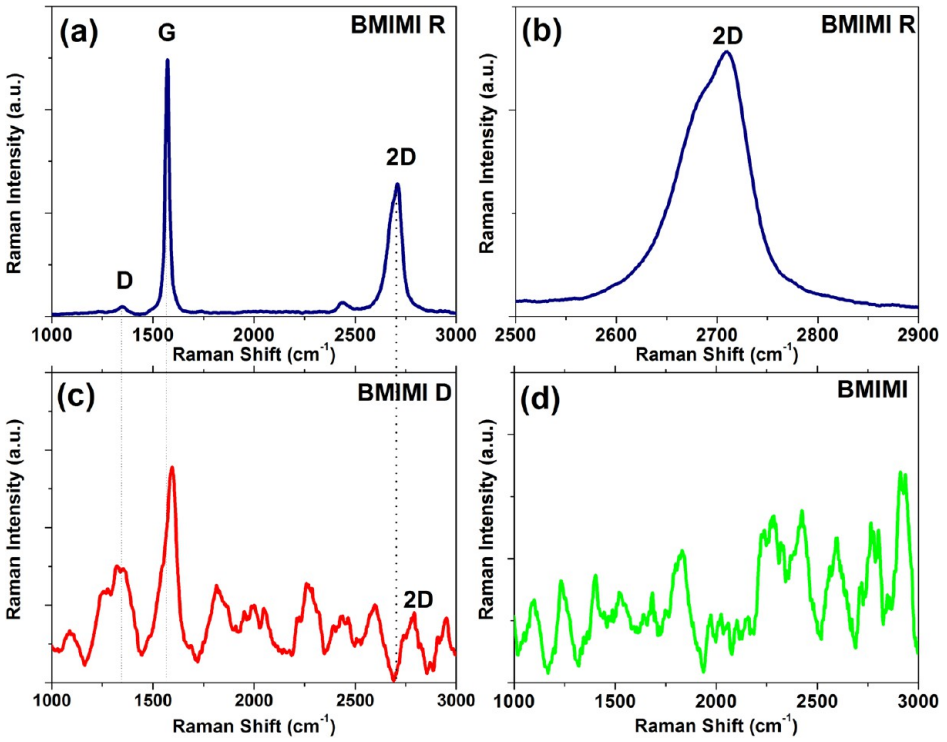

Figure 10. Raman spectrum within the friction track of (a) BMIMI R showing the presence of graphene. (b) Asymmetric G band from the spectrum (a) indicates that graphene is 4−5 layers thick. (c) Raman spectrum of BMIMI D showing the presence of graphene and IL. (d) Raman spectrum of BMIMI showing the presence of IL.

reported by Ferrari,[10] the 2D band is perfectly symmetrical for single- layer graphene, while graphite exhibits a two component $2D_1$ and $2D_2$.[13,14] As the number of layers increase, the asymmetry of the 2D peak in graphene increases, and after five layers, it is difficult to distinguish between graphene layers and graphite. In the present work, a slight asymmetry is visible (Figure 10b), which indicates that graphene is observed in a tribotrack of 4−5 layers. Raman spectrum within the track of BMIMI D (Figure 10c) exhibits the D and G bands typical of graphene. However, the 2D band can be seen shifted due to the presence of strain. Figure 10d shows the Raman spectrum taken from the track of BMIMI.

3.6. Structural−Microstructural and Chemical Information of Wear Particles. *3.6.1. Observations of Morphological Differences in Various Cycles for the Three Materials.* Figure 11 shows the transmission electron micrographs of the wear particles of BMIM I for various cycles. It is evident from Figure 11a and b that nanosized wear is the prominent feature of BMIMI in cycle 2. However, spherical shape individual particles (5−30 nm) are dominant in cycle 2, but some clustered particles in various morphologies such as linear chain elongated spherical (∼240 nm) or snowflake-like (∼400 nm) are also visible in Figure 11b. The individual particles are well dispersed as shown in Figure 11a. Interestingly, Figure 11a, inset I6, suggests the propulsion mechanism operates for individual particle formation while the insets of Figure 11b suggest the coalescence of the individual particles forms various clustered morphologies. Further, in cycle 3 of BMIMI, huge micrometer-sized clusters of large wear chunks are clearly observed (Figure 11c). A typical micrograph of the wear chunks is shown in Figure 11e. Cycle 3 also exhibits relatively large square-shaped individual nanoparticles (25−125 nm) rather than spherical particles observed in cycle 2.

The wear behavior of BMIMI D for the three cycles is shown in Figure 12. In cycle 1, various-sized nanometeric particles are embedded in 800−1000 nm sized particles (Figure 12a), while in cycle 2, multilayered graphene occurs as clustered nanoparticles (∼28 nm) (Figure 12b). In cycle 3, porous nanomeshes of graphene are a typical feature of the wear. The porosity might be developed due to mass transfer during the friction process (Figure 12c). The BMIMI R lubricant is much more interesting as can be concluded from the friction data, and thus, the expected wear behavior should also be interesting. Figure 13 shows the typical electron micrograph for the three cycles of BMIMI R. In cycle 1, uneven mass transfer from large sheets of multilayered graphene creates the nanoscale pores on the upper layers of graphene sheets. The transfer of mass in the form of sheets and aggregated particles are confirmed in Figure 13b and inset I8 of Figure 13a.

In cycle 2 of BMIMI R, wear has two different regimes ranging from large tree-like structures with meshed surfaces (Figure 13c) to the small rolled graphene nanoparticles (Figure 13d). The details of the structure formation are described in the Supporting Information. Interestingly, cycle 3 shows micrometer-sized thin graphene sheets with small graphene particles embedded within (Figure 13e). It should be noted here that occasionally these particles form a porous clustered structure (Figure 13f). Further, as mentioned in sections 3.3 and 3.4, prolonged experiments for BMIMI R have also been performed. Therefore, the wear behavior of cycle 9 and cycle 18 have also been investigated. Figure 14a shows the wear behavior of BMIMI R at cycle 9. In this cycle, wear debris are clustered (300−400 nm) and composed of individual spherical-shaped particles (∼75 nm) that are rough at the periphery. These particles appear to be part of layered graphene sheets. However, in cycle 1, these spherical sheets appear to be

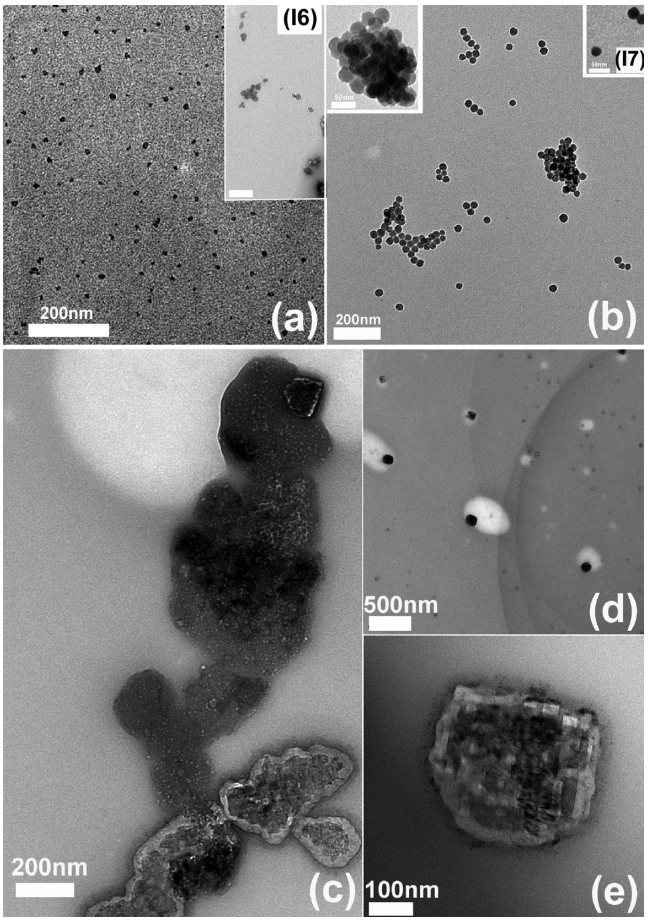

Figure 11. Transmission electron micrographs of wear particles of BMIMI I for cycle 2 showing (a) well-dispersed nanoparticles, (inset I6) propulsion mechanism for individual particles, and (b) clustered and individual spherical nanoparticles, which later contribute to a ball bearing effect with inset suggesting coalescence of individual particles to form cultured morphologies. Cycle 3 exhibiting (c) large flakes, (d) square nanoparticles, and (e) typical wear chunks.

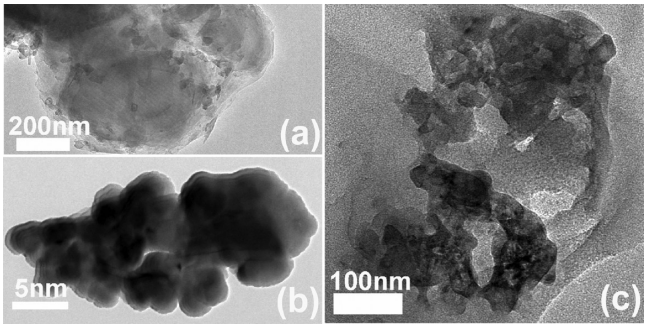

Figure 12. Typical electron micrograph of wear particles of BMIMI D (a) for cycle 1 showing embedded graphene nanoparticles, (b) for cycle 2 showing the aggregated nanoparticles, and (c) porous nanomesh in cycle 3.

exfoliated and rolled to form hollow needle-like structures as shown in Figure 14b.The individual needles are of similar size as the diameter of the particles visible in Figure 14a, which confirm that the needles are rolled exfoliated part of the individual particles of Figure 14a.

3.6.2. Structural and Chemical Behavior of the Wear from Various Cycles. To identify the presence of metal and metal oxide particles from the substrate (Al/Al_2O_3) or from the friction probe (metal−metal oxides from steel), high resolution TEM was performed on the wear samples. We present here the representative HRTEM of each sample as shown in Figure 15 as BMIMI, BMIMI D, and BMIMI R. The HRTEM investigations of cycle 2 of BMIMI D (Figure 15a) suggest the presence of graphene nanoparticles (5−10 nm) of different shapes and different edge termination. As indicated in Figure 15a, graphene nanoplatelets, zigzag edge, and armchair edge terminated particles are clearly visible. The high resolution fringes indicate that interlayer distance is ∼0.24 nm, which is the distance between two C−C atom. Interestingly, in cycle 3 of BMIMI D along with the edge termination, the atomic level defects are also generated (Figure 15b). In addition, clear boundaries between the nanodomains disappear probably due to the random rearrangement of particles overlapping each other.

Furthermore, Figure 15c is the HRTEM micrograph of wear debris in cycle 3 of BMIMI R. The HRTEM image suggests the presence of a continuous film composed of few layers of graphene sheets to bilayer graphene sheets.

From the detailed analysis of the wear particles from cycle 2 of BMIMI, it can be inferred that aluminum is worn out during the friction test. Figure 15d shows the presence of a (002) type of plane of fcc aluminum with a lattice parameter a = 0.402 nm. These observations are in accordance with the elemental analysis performed by energy dispersive X-ray analysis.

In order to determine the elemental compositions of the wear particles for all the materials, all the cycles were subjected to EDAX analysis. For the majority of samples, EDAX suggests the presence of mainly carbon due to graphene as well as IL. We were also interested to know the wear of the aluminum substrates and steel probe. It has been inferred from the EDAX analysis of the majority of wear samples that the wear of aluminum as well as the steel probes is very low. In addition, the EDAX analysis in local regions taken from the EDAX detector attached to TEM suggests that BMIMI D exhibits small amounts of aluminum, while for BMIMI R, there is no trace of aluminum. Further details are provided in Figure S5 of the Supporting Information.

4. DISCUSSION

The tribological properties of potentially useful nanohybrid lubricants have been investigated in the present study. The work here deals with tribology of steel over aluminum and the effective use of nanohybrid materials to aid lubrication between the surfaces of both metals. The effectiveness of the nanohybrid lubricant was assessed by referencing it against free ionic liquid. It has been shown previously that the FC of steel over aluminum occurs in the range of 0.5−0.45. In the present work, all three lubricants investigated were able to reduce FC and roughness significantly within the range of 0.25−0.15. The increment in FC, MFC, and roughness can directly be correlated with surface energy and the morphology of the particle within the friction tracks. It has been reported for multilayered materials and nanoparticles that the three main mechanisms, namely, rolling, sliding, and exfoliation and film transfer, play important roles in reduction of friction and wear.[15−18] In the present study, we have observed that the three lubricants under investigation reduced the FC and roughness from 0.5 to 0.1. However, BMIMI R in particular showed superior lubricating properties, and these characteristics as previously demonstrated can be correlated with low surface

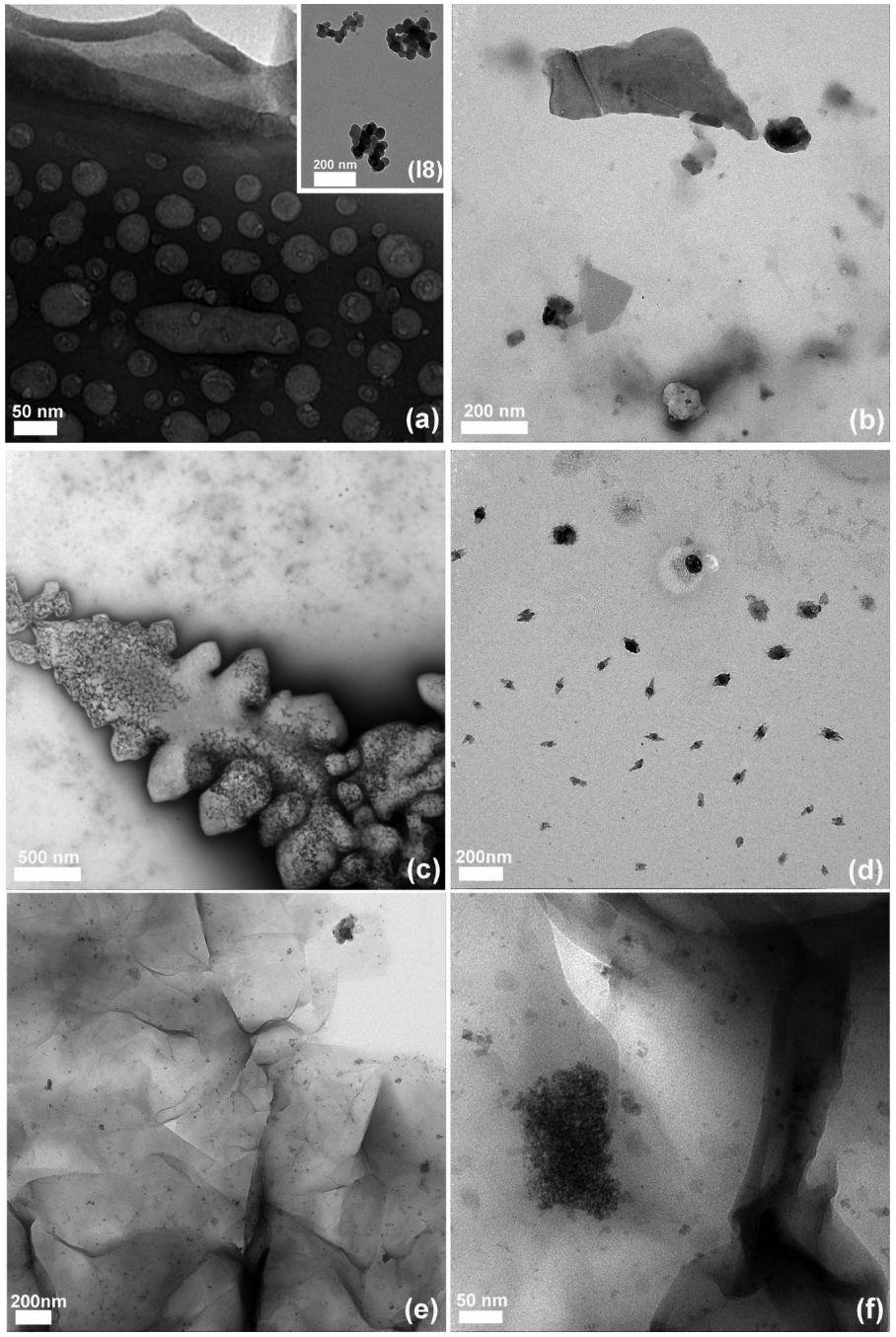

Figure 13. Typical electron micrograph of wear particles of BMIMI R showing (a) cycle 1 porosity in the top layers of graphene with inset showing particles free from the sheet to form porous graphene sheets, (b) nanosheets of graphene, (c) in cycle 2, tree-like structure and (d) rolled graphene particles, and (e,f) wrinkled graphene sheets in cycle 3.

energy and microstructural variation with the sliding distance. The variation in the lubricating properties in BMIM I with distance (cycles 1−3) may be attributed to the presence of micrometer-sized aggregates and nanoparticles. In cycle 1, the FC was observed to increase with distance, which may be explained by the initial formation of IL films on the surface that are later removed locally through the formation of micrometer-sized flat aggregates leading to an increase in FC and roughness. The formation of micrometer-sized aggregates may be assisted by the local IL environment functioning as a dispersant, which is well documented for metal and metal carbides.[9,19] In cycle 2, the morphological changes are seen to occur from micro-sized snowflakes to thinner particles but larger-sized aggregates. In this case, these snowflakes aid lubrication by forming individual nanoparticles or nanoclustures via a two-step process where dispersion of snowflakes in the individual particles within the liquid are followed by the propelling out process due to pressure during the friction test. This hypothesis is further confirmed by the TEM images of wear particles (Figure 11a,b, inset I6). Further, these individual nanoparticles are of spherical shaped and aid lubrication via a rolling mechanism between the two contact surfaces thereby by acting as "ball bearings" to reduce the FC and roughness. In cycle 3, formation of nanoparticles and thicker branched aggregates are visible.

dx.doi.org/10.1021/am302761c | ACS Appl. Mater. Interfaces 2013, 5, 4063−4075

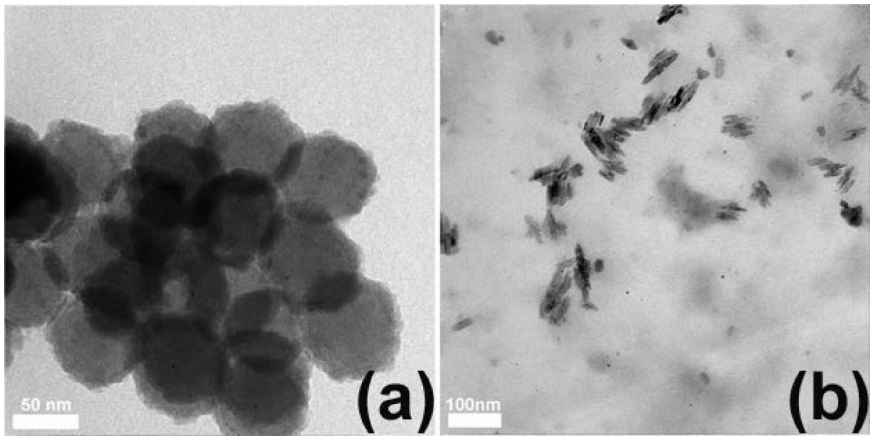

Figure 14. Wear debris of (a) cycle 9 exhibiting aggregated nanoparticles and (b) cycle 18 showing hollow needles generated by exfoliation and rolling of nanoparticles/nanosheets.

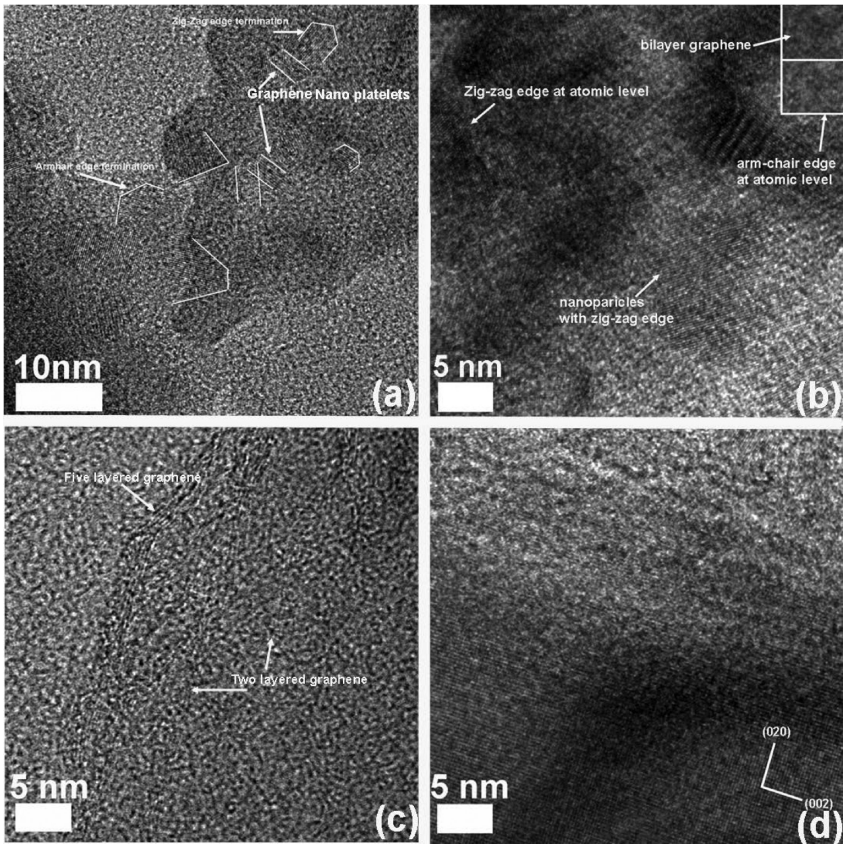

Figure 15. High resolution TEM micrograph of wear particles of (a) BMIMI D in cycle 2 showing the presence of edge terminated graphene nanoparticles, (b) BMIMI D in cycle 3 showing edge termination at atomic level, (c) BMIMI R in cycle 3 exhibiting film of few layer graphene, and (d) BMIMI showing the presence of aluminum metal.

However, the FC is lower but still higher than cycles 1 and 2, which can be explained by the argument that the rolling (due to nanoparticles) and sliding (due to aggregates) phenomena are in direct competition with each other, but possibly due to the large thickness of aggregates, the FC increases compared to cycles 1 and 2. It is worth noting that the shape of nanoparticles is also a crucial factor. The ball bearing effect is less effective for square-shaped nanoparticles in cycle 3 (Figure 11c) than the spherical nanoparticles in cycle 2 (Figure 11b).

In case of BMIMI D, for cycle 1, the slight material transfer (local tribofilm of lubricant) helps in reducing the FC in comparison to the nonlubricating surface, but as compared to cycle 3, the FC and roughness are higher because of the presence of wear particles and also due to the complete tribofilm formation in cycle 2. In case of cycle 3, the removal of tribofilm formation of cracks and relatively large amount of wear particles diminishes the effect of easy shearing due to material transfer in the form of wear. The large variation in MFC can be attributed to the wear particles and crack formation. Additionally, the wear particles also have different morphologies that affect the friction behavior in each cycle. In cycle 1, wear particles are nanoparticles embedded in graphene

dx.doi.org/10.1021/am302761c | ACS Appl. Mater. Interfaces 2013, 5, 4063−4075

sheets resulting from material transfer and possibly providing a rougher surface and thus the friction coefficient is higher, while in case of cycle 2, the nanoparticles do not exhibit strong ball bearing-like behavior due to their shape but can to a certain extent help in reducing the friction coefficient. Interestingly, in cycle 3, the nonporous graphene wear certainly aids in increments of the friction coefficient. Moreover, HRTEM indicates an interesting aspect of variation friction between cycles 2 and 3 related with the edge effect. Interestingly, the effect of edge termination at the nanoscale by forming edge-terminated nanoparticles is helpful for reduction of wear as shown in cycle 2, but at the same time the edge termination at the atomic level increases the friction locally, which results in slight increases in the friction coefficient in cycle 3.

For BMIM R in cycle1, possibly exfoliation and the presence of graphene layers work as a separator between the two contact surfaces and thus reduces the FC (images not shown here). The exfoliation is confirmed by the presence of micro-sized graphene sheets in the wear debris. However, friction is reduced by the graphene layer acting as a separator but is insufficient due to the formation of clusters via material transfer as evidenced by the presence of porous graphene layers and clustered particles (Figure 13b and inset I8). However, in cycle 2, the material transfer phenomenon followed by adhesion of graphene flakes increases the shearing between the contact surface and thus FC increases. This is shown in Figure 9a from the rough surface and nanoscale crack formation. The wear behavior of cycle 3 clearly confirms the material transfer and adhesion phenomenon. The wear debris also suggests that material transfer and adhesion is a simultaneous process that can be attributed by the formation of tree-like morphology (Figure 13c). However, the presence of liquid helps in the formation of tree-like structures, a process evidenced by TEM experiments that reveal a change in color from black to white and also a change of texture from a smooth to rough surface upon exposure to the concentrated electron beam. This is probably due to the structure coloration change arising from the removal of liquid. The variations in microstructures are shown in the Supporting Information. Furthermore, in cycle 3, further force smoothes out the adhesive film as shown in Figure 9b, c, and d, and also the further exfoliation and material transfer eases out the shear between the two contact surfaces and thus friction reduces to the minimum. Exfoliation is further confirmed by the presence of large wrinkled graphene sheets in the wear material (Figure 13 e,f).

5. CONCLUSIONS

In summary, we conclude that [BMIM][I] and graphene/[BMIM][I] nanohybrid materials can be synthesized via an energy efficient route and can serve as effective lubricants for the steel on aluminum system in view of their tribological properties and their ability to substantially reduce friction and wear. The finding that the reduction in FC by the three lubricant systems occurs via different mechanisms as predicted by microscopy imaging offers engineers and material scientists greater selectivity and flexibility for optimizing lubrication by fine-tuning nanohybrid−IL interactions. This phenomenon is dictated by the composition of nanohybrid materials and offers the potential to tailor tribological conditions for their desired effects for different surface materials. Furthermore, a relatively low amount of aluminum and steel in the wear analysis suggests that these lubricants are better for wear properties also. From the perspective of lubrication design and modulation of frictional forces based upon the BMIM nanohybrid IL materials as a model, the current study presents opportunities to further explore the potential of machine lubrication technology.

■ ASSOCIATED CONTENT

Supporting Information

A photograph of the three samples, friction curve without smoothing the data, additional surface morphology of the friction track of BMIMI R at 9th cycle and 18th cycle, additional details on the special morphologies of wear particles of BMIMI R in cycle 3 and EDAX of wear particle showing the low content of aluminum. This material is available free of charge via the Internet at http://pubs.acs.org.

■ AUTHOR INFORMATION

Corresponding Author

*E-mail: khare@snu.ac.kr (V.K.); ahnsh@snu.ac.kr (S.-H.A.).

Notes

The authors declare no competing financial interest.

■ ACKNOWLEDGMENTS

This work was supported by the National Research Foundation of Korea (NRF) grant funded by the Korea government (MEST) (2012R1A1A2008196 and 2012-0008727). One of the authors, Dr. V. Khare, also gratefully acknowledges financial support from the BK 21 program of the government of Korea. Authors are thankful to Dr. Larisa Lee Cruz for fruitful scientific discussions. The authors gratefully acknowledge Dr. Sookyung Hwang for help with friction measurements. We sincerely thank to Dr. Sanjiv Sonkaria for careful reading of the manuscript.

■ REFERENCES

(1) Zhou, F.; Liang, Y.; Yu, L. *Chem. Soc. Rev.* **2009**, *38*, 2590−2599.
(2) Bermúdez, M. D.; Jiménez, A. E.; Sanes, J.; Carrión, F. J. *Molecules* **2009**, *14*, 2888−2908.
(3) Yao, M.; Fana, M.; Lianga, Y.; Zhoua, F.; Xia, Y. *Wear* **2010**, *268*, 67−71.
(4) Zhang, L.; Feng, D.; Xu, B. *Tribol. Lett.* **2009**, *34*, 95−101.
(5) Jin, C. M.; Ye, C.; Phillips, B. S.; Zabinski, J. S.; Liu, X.; Liud, W.; Shreeve, J. M. *J. Mater. Chem.* **2006**, *16*, 1529−1535.
(6) Sanes J, C. F.; Bermúdez, M. D.; Arribas, A. *Tribol. Lett.* **2010**, *41*, 199−207.
(7) Pu, J.; Wan, S.; Zhao, W.; Mo, Y.; Zhang, X.; Wang, L.; Xue, Q. *J. Phys. Chem. C* **2011**, *115*, 13275−13284.
(8) Khare, V.; Ruby, C.; Sonkaria, S. *IJPEM* **2012**, *13*, 1207−1213 , special issue on green manufacturing.
(9) Khare, V.; Kraupner, A.; Mantion, A.; Jelicic, A.; Thünemann, A. F.; Giordano, C.; Taubert, A. *Langmuir* **2010**, *26*, 10600−10605.
(10) Ferrari, A. C. *Solid State Commun.* **2007**, *143*, 47−57.
(11) Hernandez, Y.; Nicolosi, V.; Lotya, M.; Blighe, F. M.; Sun, Z.; De, S.; McGovern, I. T.; Holland, B.; Byrne, M.; Gun'Ko, Y. K.; Boland, J. J.; Niraj, P.; Duesberg, G.; Krishnamurthy, S.; Goodhue, R.; Hutchison, J.; Scardaci, V.; Ferrari, A. C.; Coleman, J. N. *Nat. Nanotechnol.* **2008**, *3*, 563−568.
(12) Ferrari, A. C.; Meyer, J. C.; Scardaci, V.; Casiraghi, C.; Lazzeri, M.; Mauri, F.; Piscanec, S.; Jiang, D.; Novoselov, K. S.; Roth, S.; Geim, A. K. *Phys. Rev. Lett.* **2006**, *97*, 187401.
(13) Nemanich, R. J.; Solin, S. A. *Phys. Rev. B: Condens. Matter Mater. Phys.* **1979**, *20*, 392−401.
(14) Vidano, R. P.; Fishbach, D. B.; Willis, L. J.; Loehr, T. M. *Solid State Commun.* **1981**, *39*, 341−344.
(15) Teveta, O.; Huthb, P. V.; Birob, R. P.; Rosentsveiga, R.; Wagnera, H. D.; Tennea, R. *Proc. Natl. Acad. Sci. U.S.A.* **2011**, *108*, 19901−19906.

(16) Tenne, R.; Margulis, L.; Genut, M.; Hodes, G. *Nature* **1992**, *360*, 444−446.
(17) Greenberg, R.; Halperin, G.; Etsion, I.; Tenne, R. *Tribol. Lett.* **2004**, *17*, 179−186.
(18) Wu, J. F.; Zhai, W. S.; Jie, G. F. *Proc. - Inst. Mech. Eng.* **2009**, *223*, 695−703.
(19) Khare, V.; Li, Z.; Mantion, A.; Ayi, A. A.; Sonkaria, S.; Voelkl, A.; Thünemann, A. F.; Taubert, A. *J. Mater. Chem.* **2010**, *20*, 1332−1339.